Heliyon 9 (2023) e22537

Contents lists available at ScienceDirect

Heliyon

journal homepage: www.cell.com/heliyon

Effect of Zr_3Fe addition on hydrogen storage behaviour of Ti_2CrV alloys

Daniela Bellon Monsalve [a,b,*], Elena Ulate-Kolitsky [c], Alejandro-David Martínez-Amariz [b], Jacques Huot [a]

[a] Hydrogen Research Institute, Université Du Québec à Trois-Rivières, QC, G9A 5H7, Canada
[b] Universidad de Santander, Facultad de Ingenierías y Tecnologías, Instituto de Investigación Xerira, Bucaramanga, Colombia
[c] Centre de Métallurgie du Québec, 3095 Rue Westinghouse Parc Industriel Des Hautes-Forges, Trois-Rivières, Québec, G9A 5H7, Canada

ARTICLE INFO

Keywords:
Hydrogen storage
Metal hydrides
TiCrV system
Crystal structure
X-ray diffraction

ABSTRACT

In this work, the hydrogen storage behavior of Ti_2CrV + X wt.% Zr_3Fe, where X = 2, 4, 6, 8 and 10 was investigated. The synthesis of all samples was carried out through arc-melting, followed by comprehensive characterization using X-ray diffraction, scanning electron microscopy, and energy-dispersive spectroscopy. The pure-Ti_2CrV as-cast sample presented a single-phase microstructure. However, the addition of the Zr_3Fe led to a remarkable transformation, resulting in the appearance of a Zr-rich secondary phase. It was found that the first hydrogenation is improved with the addition of at least 6 wt% of Zr_3Fe, avoiding any preheating of the sample. These samples achieved their maximum capacity in approximately 10 min at room temperature. The maximum capacity recorded was 4.2 wt% H for the sample with X = 6 wt% Zr_3Fe, while for X = 8 and 10 wt % Zr_3Fe, the capacity recorded was 4.1 wt% and 4.0 wt%, respectively.

1. Introduction

In the last decade, there has been a growing interest towards the hydrogen economy as a promising option to decarbonize a wide range of sectors, as well as to diversify the energy matrix and to strengthen countries' energy security [1–3]. However, its storage remains the main barrier to its wide utilization. Several approaches to store hydrogen safely and with acceptable rates of absorption and desorption have been investigated, among which physical storage and chemical storage stand out [4–6].

Metal hydrides are considered appealing materials for hydrogen storage owing to their high volumetric density, safety, no toxicity emission, along with their effective uptake and release capacities [7–9]. However, some of the most common barriers to their application are related to low gravimetric hydrogen density, limited cyclability, non-reversibility, high cost, and complex activation processes. Several alloys have been studied, and different methods have been developed to overcome those drawbacks, such as microstructural lattice defects creation [10,11], alloying substitution [12,13], or use of additives [14–16].

Ti–V-based system forms body-centered cubic solid solution alloys, which show great potential for real-world hydrogen storage applications due to their relatively good hydrogen storage capacity as well as a remarkably rapid reactivity with hydrogen [17]. Both Ti and V have the individual ability to readily absorb significant amounts of hydrogen. Titanium can attain its highest hydrogen content of 3.78 wt%, while vanadium can uptake as much as 5.94 wt% H [18]. It is widely recognized that Ti and V are capable of

* Corresponding author. Hydrogen Research Institute, Université Du Québec à Trois-Rivières, QC, G9A 5H7, Canada.
E-mail addresses: daniela.bellon@uqtr.ca, dan.bellon@mail.udes.edu.co (D. Bellon Monsalve).

https://doi.org/10.1016/j.heliyon.2023.e22537
Received 28 July 2023; Received in revised form 2 November 2023; Accepted 14 November 2023
Available online 21 November 2023

forming solid solutions at various ratios, and these solutions exhibit hydrogen-reactive behavior without undergoing disproportionation [18]. However, these alloys have been associated with certain noticeable limitations, including a limited release capacity and a complex first-hydrogenation process. To enhance the effectiveness of these alloys, researchers have investigated the impact of incorporating another element such as Cr, Mn, and Fe [19]. In this regard, Ti–V compounds form the basis of alloys such as Ti–V–Fe, Ti–V–Mn, and Ti–V–Cr, which have a body-centered cubic structure and typically exhibit a high gravimetric hydrogen storage capacity (3.8 wt%) [20–23].

Ti–V–Cr alloys are a specific subset within the Ti–V-X system, where chromium is the third alloying element. Extensive research has been conducted on the TiVCr-based system [24–27], and is regarded as extremely favorable for hydrogen storage because of its crystal structure (BCC), which enables hydrogen diffusion at relatively modest operational conditions (temperature and pressure) [28]. Additionally, it offers a superior storage capacity in comparison to conventional systems such as AB_x (X = 1, 2, 5) [29]. This makes the alloys of this system interesting candidates for hydrogen storage applications [16,30]. However, their ability to reversibly store

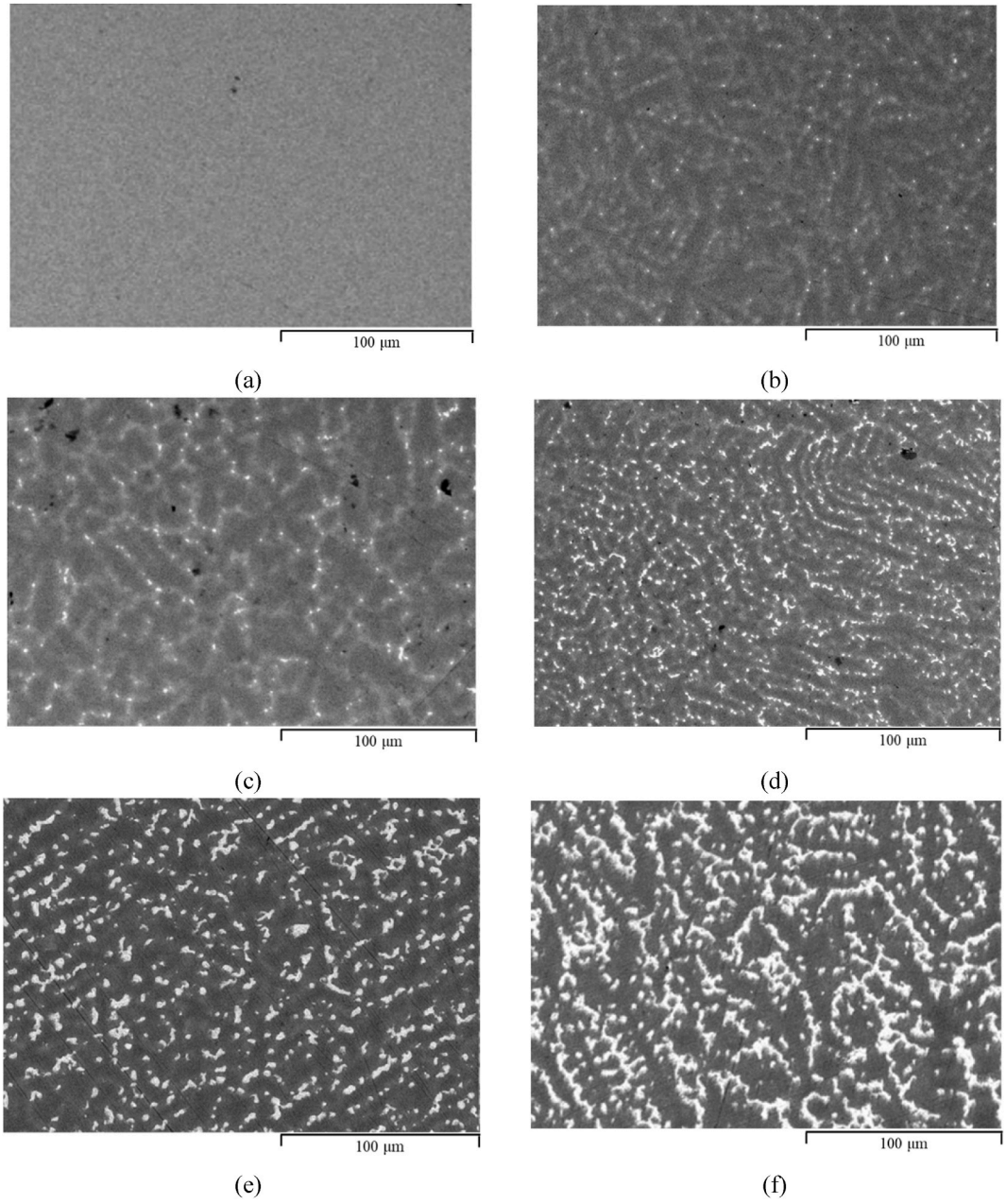

Fig. 1. Backscattered electrons image of (a) Ti_2CrV, (b) Ti_2CrV + 2 % Zr_3Fe, (c) Ti_2CrV + 4 % Zr_3Fe, (c) Ti_2CrV + 6 % Zr_3Fe, (e) Ti_2CrV + 8 % Zr_3Fe, (f) Ti_2CrV + 10 % Zr_3Fe.

hydrogen is diminished, primarily as a result of the monohydride's low plateau pressure. Additionally, long incubation times have been reported during their first hydrogenation [31–33].

Within the Ti–Cr–V alloy series, Ti_2CrV has the highest hydrogen absorption capacity [34]. Kumar et al., and more recently Huazhou et al. reported the maximum absorption capacity of Ti_2CrV of more than 4.1 wt% at room temperature [27,35]. Nevertheless, the capacity for reversible storage remains limited. Also, the activation process requires temperatures of 400 °C [35]. Other studies have analyzed the cyclability of the alloy and reported enhancements in hydrogen storage behavior through the addition of elements like Mo, Fe, Co, and Ni [16–18].

Zr–Fe intermetallic compounds have been shown to improve the hydrogen storage properties such as kinetics and hydrogen storage capacity, when added to the main alloy [28]. As a result, this system is the focus of comprehensive research [36–40]. In the case of Zr_3Fe, it has an absorption capacity of 2.0 wt% at room temperature and low pressure, it could be considered a suitable option for stationary hydrogen-based applications [36].

In the present work, the effect on the crystal structure, microstructure and first hydrogenation behavior of the addition of Zr_3Fe to the Ti_2CrV alloy was studied. Specifically, compositions Ti_2CrV + X wt.% Zr_3Fe (X = 0, 2, 4, 6, 8 and 10) were investigated.

2. Experimental details

All the elements Ti (99.95 %), Cr (99 %), V (99.7 %), Zr (99.5 %), and Fe (99.99 %) were purchased from Alpha Aesar®. All materials were mixed in the specified quantities and subsequently synthesized through arc-melting in an argon atmosphere to prevent oxidation. During the melting process, each pellet underwent four consecutive turnovers and remelting to achieve homogeneity.

The material characterization was carried out using different techniques. To study the morphology of the samples, Scanning Electron Microscope (SEM) was carried out in a Hitachi VP-SEM SU1510 in the backscattering mode (BSE). To probe the chemical composition of the samples the Energy Dispersive Spectroscopy (EDS) was used (Oxford Instrument X-Max 20 mm^2 column). To investigate the sample's crystal structure, X-ray diffraction (XRD) measurements were conducted using a D8 Focus Bruker X-ray powder diffractometer with Cu Ka radiation. The XRD patterns were then subjected to analysis through the Rietveld method, employing TOPAS software to identify phase composition, lattice parameters, microstrain, and crystallite size of the alloys [41].

The hydrogen sorption and desorption behavior were studied using a homemade Sievert-type apparatus. The synthesized samples were manually crushed within an argon-filled glove box, employing a hardened mortar and pestle. It should be noted that there was no specific control over the particle size after the crushing step. The first hydrogenation (activation) procedure for all samples was done under 2000 kPa of hydrogen pressure at room temperature (RT). Pure-Ti_2CrV, that did not activate at room temperature, underwent an activation heat treatment at 400 °C under dynamic vacuum for 1 h.

3. Results and discussion

3.1. Morphology

Fig. 1(a–f) shows the backscattered electron images obtained by SEM of the as-cast samples. Fig. 1(a) shows the pure-Ti_2CrV alloy, the microstructure is uniform but there is some change of grey shade. Fig. 1(b–f) show the presence of regions with different shades of grey and also bright regions when Zr_3Fe is added. As the amount of Zr_3Fe rises, the relative surface area of the bright region increases as it can be observed for the x = 6, 8, and 10 wt% compositions. Table 1 shows the overall chemical composition of the samples measured by EDS and is compared to the nominal composition. The recorded values for most samples are close to the nominal compositions.

Table 2 displays the chemical composition of each area as determined by EDS. The relative amount of each region was calculated by image analysis, The overall composition of the matrix region is essentially the same for all alloys. On the other hand, the composition of the bright region is Zr-rich and varies between samples. The bright region for X = 2 and 4 wt% has a similar composition ~25 at. % Zr, 14 at. % Cr, 12 at. % V and 46 at. % Ti. Similarly, the compositions of the bright region for X = 6, 8, and 10 wt% samples are very close:

Table 1
Chemical composition, in at. %, of the samples EDS analysis (uncertainty is ±0.2 for all values).

Alloy		Chemical composition (at. %)				
		Ti	V	Cr	Zr	Fe
Ti_2CrV	Nominal value	50.0	25.0	25.0	–	–
	Measured value	53.1	25.3	21.5	–	–
Ti_2CrV +2 % Zr_3Fe	Nominal value	49.4	24.7	24.7	0.9	0.3
	Measured value	51.2	24.6	22.0	1.8	0.4
Ti_2CrV +4 % Zr_3Fe	Nominal value	48.8	24.4	24.4	1.8	0.6
	Measured value	50.6	23.3	23.1	2.1	0.8
Ti_2CrV +6 % Zr_3Fe	Nominal value	48.2	24.1	24.1	2.6	0.9
	Measured value	49.1	23.5	23.3	3.0	1.0
Ti_2CrV +8 % Zr_3Fe	Nominal value	47.7	23.8	23.8	3.5	1.2
	Measured value	47.7	24.1	22.4	4.4	1.3
Ti_2CrV +10 % Zr_3Fe	Nominal value	47.1	23.6	23.6	4.3	1.4
	Measured value	47.0	23.3	22.8	5.2	1.7

Table 2
Chemical composition, in at. % of the matrix and bright region from EDS analysis (uncertainty is ±0.2 for all values).

Alloy	Region	Area (%)	Chemical composition (at. %)				
			Ti	V	Cr	Zr	Fe
Ti_2CrV	Matrix	100	53.1	25.3	21.5	–	–
		–	–	–	–	–	–
Ti_2CrV +2 % Zr_3Fe	Matrix	98	50.6	25.4	22.3	1.4	0.3
	Bright region	2	45.7	13.7	15.9	23.7	0.6
Ti_2CrV +4 % Zr_3Fe	Matrix	96	50.1	25.0	23.0	1.2	0.6
	Bright region	4	47.4	11.4	13.3	27.1	0.6
Ti_2CrV +6 % Zr_3Fe	Matrix	93	47.3	26.4	24.0	1.5	0.8
	Bright region	7	41.2	17.1	25.6	13.6	2.4
Ti_2CrV +8 % Zr_3Fe	Matrix	87	47.5	26.1	23.0	2.4	1.1
	Bright region	13	42.6	17.3	22.7	14.9	2.4
Ti_2CrV+10 % Zr_3Fe	Matrix	77	48.1	24.5	23.4	2.6	1.3
	Bright region	23	39.1	18.0	25.7	14.2	3.0

~14 at. % Zr, 25 at. % Cr, 17 at. % V, 41 at. % Ti and 2 at. % Fe.

3.2. Effect of Zr_3Fe on first hydrogenation

Fig. 2(a) shows the activation curves at room temperature and 2000 kPa for the different samples from 0 to 10 wt% of Zr_3Fe. After 24 h, the X = 2 and 4 wt% samples did not absorb hydrogen while the 6, 8 and 10 wt% samples showed good first hydrogenation kinetics. The maximum capacity achieved was 4.2 wt% for X = 6, although this composition exhibits slower kinetics than X = 8 and 10, the full hydrogenation is still reached within 10 min. A hydrogen absorption capacity of 4.1 wt% and 4.0 wt% was registered for X = 8 and 10, respectively. It can be correlated with how the absorption capacity slightly decreases as the amount of Zr_3Fe increases. Nevertheless, we see that the addition of at least 6 % of Zr_3Fe is required to improve the first hydrogenation kinetics and therefore avoid the heat treatment step at high temperature before activation.

The activation curve of the composition with 10 wt% Zr_3Fe has two distinct steps: one between 2.8 and 3 wt%, the other between 3.65 and 3.85 wt%. A similar behaviour is seen for the 6 wt% Zr_3Fe but at different capacities and is practically inexistent for 8 wt% Zr_3Fe (see Fig. 2(b)).

3.3. Effect of heat treatment

As the sample without Zr_3Fe could not activate at RT, we investigated the effect of a prior heat treatment. Fig. 3 shows the activation at room temperature of a Ti_2CrV sample after a heat treatment at 400 °C for 1 h under vacuum. When the sample is heated before hydrogenation, the absorption is complete in less than 1 h.

3.4. Crystal structure

Fig. 4 shows the XRD patterns of as-cast samples. All as-cast samples present a single-phase BCC structure. However, the SEM/EDX

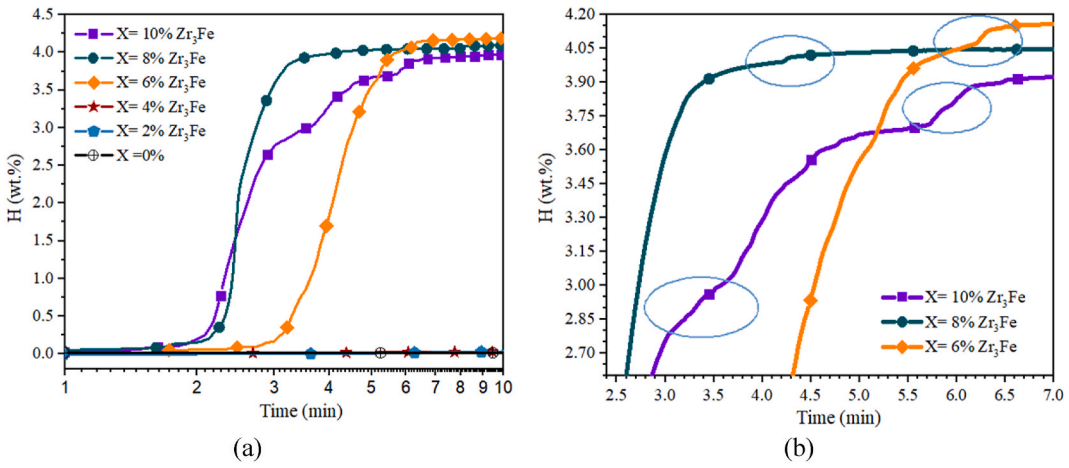

Fig. 2. Ti_2CrV + X% Zr_3Fe (X = 0, 2, 4, 6, 8, and 10) (a) activation at 2000 kPa H pressure and RT, without heating, (b) Detailed look at the change of slope in hydrogenated samples.

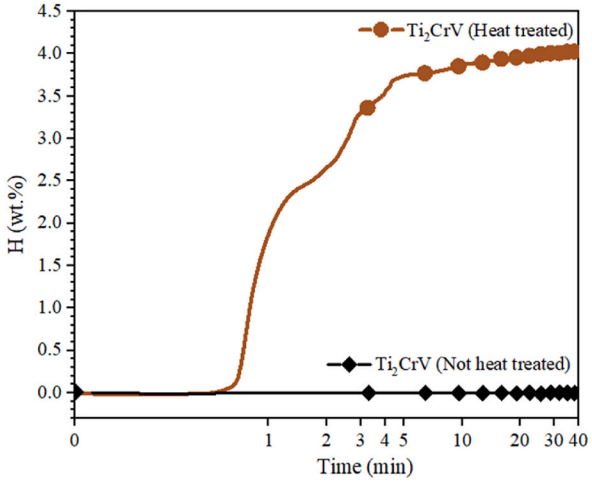

Fig. 3. The Ti_2CrV first hydrogenation at 2000 kPa of hydrogen pressure and RT with and without heating.

investigation shows the presence of two distinct regions: grey and bright. This is particularly troublesome for the 10 % Zr_3Fe pattern which has 23 % of the bright phase by area. From the EDX analysis, it is evident that the bright phase is zirconium-rich. Zirconium has a much bigger atomic radius than the other atoms and thus, the formation of a Laves phase is possible. However, the amount of zirconium is too small to reach the AB_2 stoichiometry. Therefore, a BCC structure is adopted instead. To confirm this, we computed the average atomic radius for the grey and bright regions for all compositions. The results are shown in Table 3. From this table it is possible to see that the average atomic radius for the grey region is almost the same, for all compositions. For the bright region, there is a general trend of decreasing average atomic radius with increasing Zr_3Fe addition. The maximum difference of average atomic radius is about 4 %. Therefore, it could be expected that, if the bright region also has a BCC structure, then the lattice parameter will differ by only 4 % compared to the BCC of the grey region. However, such a difference in the lattice parameter means a difference of almost two degrees for the (1 1 0) peak at around 41° and a difference of almost 4° for the (2 2 0) peak at around 88°. Clearly, this is not what is seen in the diffraction patterns of Fig. 4. Therefore, further analysis such as synchrotron diffraction is planned to provide deeper insights into the structural differences observed.

The crystallographic parameters of the samples in their as-cast state are presented in Table 4. All samples have comparable "a" lattice parameter and microstrain. The crystallite size is roughly constant up to x = 6 wt%. When the proportion of Zr_3Fe further increases the crystallite size decreases.

Fig. 5 shows the XRD patterns of the samples after hydrogenation at room temperature. The samples with X = 0, 2, and 4 wt% that did not activate showed only a BCC structure. The 6, 8, and 10 wt% Zr_3Fe samples all presented FCC structures after activation. It is a widely recognized fact that the hydrided form of a BCC alloy becomes FCC. Therefore, the emergence of the FCC phase can be directly attributed to the existence of the BCC phase in the as-cast condition. Table 5 shows the crystallographic parameters after activation. We see that, for the samples that did not absorb hydrogen, the BCC lattice parameters are practically the same as in the as-cast state. The microstrains are also the same. This means that hydrogen did not even enter in a solid solution for these compositions. For the alloys that did absorb hydrogen, we see that the crystallite size is slightly smaller, while there is an increase in the microstrain.

4. Conclusions

The effect of Zr_3Fe addition on first hydrogenation kinetics (activation) of Ti_2CrV alloy was investigated. Samples with less than 6 wt% Zr_3Fe did not activate at room temperature but, for higher proportion of Zr_3Fe the alloys fully absorbed in less than 10 min. All samples were single-phase BCC despite showing regions with distinct chemical compositions mainly differing by the zirconium content. A fast first hydrogenation could also be achieved by heat treating the sample at high temperature under vacuum.

Data availability statement

Data included and referenced in article. Additional data will be available on request.

CRediT authorship contribution statement

Daniela Bellon Monsalve: Writing – review & editing, Writing – original draft, Visualization, Validation, Resources, Project administration, Methodology, Investigation, Funding acquisition, Formal analysis, Data curation, Conceptualization. **Elena Ulate-Kolitsky:** Writing – review & editing, Validation, Supervision, Formal analysis. **Alejandro-David Martínez-Amariz:** Writing – review & editing, Supervision. **Jacques Huot:** Writing – review & editing, Validation, Supervision, Resources, Project administration,

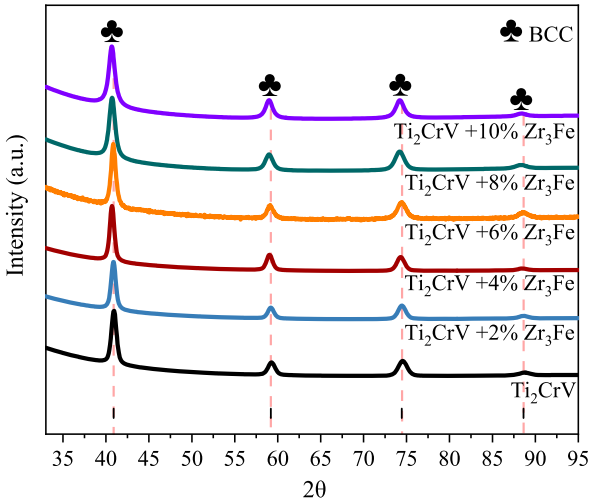

Fig. 4. XRD patterns of as-cast samples Ti_2CrV + X% Zr_3Fe (X = 0, 2, 4, 6, 8, 10). Diffraction peaks: black for Ti_2CrV, pink for Zr_3Fe. (For interpretation of the references to colour in this figure legend, the reader is referred to the Web version of this article.)

Table 3
Average atomic radii (in Å) of samples in as-cast state.

Region	X = 0	X = 2	X = 4	X = 6	X = 8	X = 10
Grey region	1.404	1.406	1.404	1.400	1.403	1.403
Bright region	–	1.451	1.468	1.421	1.426	1.419

Table 4
Crystallographic parameters of the as-cast samples. The number in parentheses is the uncertainty on the last significant digit.

Alloy	Rwp	a (Å)	V (Å^3)	Crystallite size (nm)	Microstrain (%)
Ti_2CrV	4.27	3.1190 (7)	30.34 (2)	17.4 (1)	0.27 (1)
Ti_2CrV + 2 % Zr_3Fe	3.99	3.1216 (6)	30.42 (2)	16.4 (8)	0.21 (8)
Ti_2CrV + 4 % Zr_3Fe	4.93	3.1190 (7)	30.34 (2)	18.8 (1)	0.23 (9)
Ti_2CrV + 6 % Zr_3Fe	2.21	3.1236 (4)	30.48 (1)	16.0 (4)	0.25 (4)
Ti_2CrV + 8 % Zr_3Fe	2.77	3.1286 (5)	30.62 (1)	10.4 (2)	0.24 (7)
Ti_2CrV + 10 % Zr_3Fe	2.84	3.1246 (5)	30.51 (2)	8.0 (2)	0.12 (1)

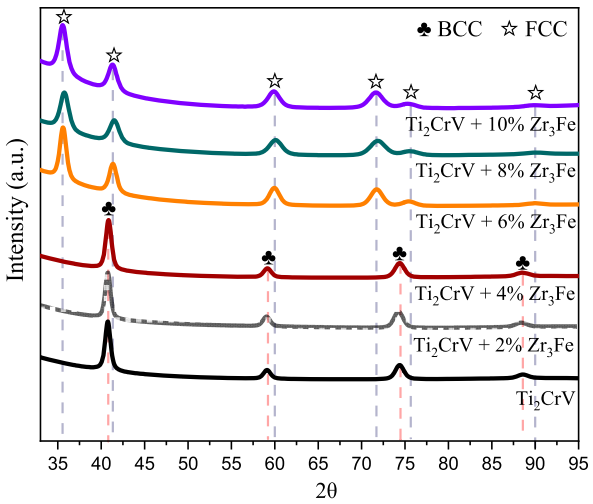

Fig. 5. XRD patterns of hydrogenated samples Ti_2CrV + X% Zr_3Fe (X = 0, 2, 4, 6, 8, 10).

Table 5
Crystallographic parameters of the activated samples. The number in parentheses is the uncertainty on the last significant digit.

Alloy	Rwp	Phase	a (Å)	V (Å^3)	Crystallite size (nm)	Microstrain (%)
Ti_2CrV	6.29	BCC	3.1190 (1)	30.34 (3)	12.7 (8)	0.22 (1)
Ti_2CrV + 2 % Zr_3Fe	6.03	BCC	3.1221 (8)	30.43 (2)	14.1 (8)	0.22 (1)
Ti_2CrV + 4 % Zr_3Fe	6.31	BCC	3.1247 (1)	30.51 (3)	14.3 (1)	0.28 (1)
Ti_2CrV + 6 % Zr_3Fe	5.79	FCC	4.364 (2)	83.09 (1)	11.6 (1)	0.38 (2)
Ti_2CrV + 8 % Zr_3Fe	5.54	FCC	4.366 (3)	83.23 (2)	8.3 (8)	0.46 (2)
Ti_2CrV + 10 % Zr_3Fe	5.86	FCC	4.368 (3)	83.34 (2)	8.0 (7)	0.40 (3)

Investigation, Funding acquisition, Formal analysis, Conceptualization.

Declaration of competing interest

The authors declare that they have no known competing financial interests or personal relationships that could have appeared to influence the work reported in this paper.

References

[1] International Energy Agency, The Future of Hydrogen: Seizing Today's Opportunities, no. June, IEA Publ., 2019, p. 203 [Online]. Available: https://www.iea.org/reports/the-future-of-hydrogen.
[2] J. E Garzon, D Bellon, A Proposal for the Transformation of Fossil Fuel Energy Economies to Hydrogen Economies Through Social Entrepreneurship, in: J. Gamez-Gutierrez, J. Saiz-Alvarez (Eds.), Entrepreneurial Innovation for Securing Long-Term Growth in a ShortTerm Economy, IGI Global, 2021, pp. 48–70. https://doi.org/10.4018/978-1-7998-3568-4.ch004.
[3] JE Garzón Baquero, D Bellon Monsalve, From fossil fuel energy to hydrogen energy: transformation of fossil fuel energy economies into hydrogen economies through social entrepreneurship, Int. J. Hydrogen Energy (2023) 48–70, https://doi.org/10.1016/j.ijhydene.2023.06.123.
[4] N. Ma, W. Zhao, W. Wang, X. Li, H. Zhou, Large scale of green hydrogen storage : opportunities and challenges, Int. J. Hydrogen Energy (2023) 1–18, https://doi.org/10.1016/j.ijhydene.2023.09.021.
[5] V. Aranda, D. Rodrigo, J. Huot, W. Jos, G. Zepon, Hydrogen storage properties of the TiVFeZr multicomponent alloy with C14-type laves phase structure. 162 (August), Intermetallics 162 (August) (2023) 1–7, https://doi.org/10.1016/j.intermet.2023.108020.
[6] L. Luo, et al., High-entropy alloys for solid hydrogen storage: a review, Int. J. Hydrogen Energy (2023) 1–25, https://doi.org/10.1016/j.ijhydene.2023.07.146.
[7] M.M. Nygård, G. Ek, D. Karlsson, M. Sahlberg, M.H. Sørby, B.C. Hauback, Hydrogen storage in high-entropy alloys with varying degree of local lattice strain, Int. J. Hydrogen Energy 44 (55) (2019) 29140–29149, https://doi.org/10.1016/j.ijhydene.2019.03.223.
[8] S.K. Chen, P.H. Lee, H. Lee, H.T. Su, Hydrogen storage of C14-CruFevMnwTixVyZrz alloys, Mater. Chem. Phys. 210 (2018) 336–347, https://doi.org/10.1016/j.matchemphys.2017.08.008.
[9] K. Benyelloul, L. Seddik, Y. Bouhadda, M. Bououdina, H. Aourag, K. Khodja, Effect of pressure on structural, elastic and mechanical properties of transition metal hydrides Mg7TMH16 (TM = Sc, Ti, V, Y, Zr and Nb): first-principles investigation, J. Phys. Chem. Solid. 111 (May) (2017) 229–237, https://doi.org/10.1016/j.jpcs.2017.08.001.
[10] K. Edalati, H. Shao, H. Emami, H. Iwaoka, E. Akiba, Z. Horita, Activation of titanium-vanadium alloy for hydrogen storage by introduction of nanograins and edge dislocations using high-pressure torsion, Int. J. Hydrogen Energy 41 (21) (2016) 8917–8924, https://doi.org/10.1016/j.ijhydene.2016.03.146.
[11] K. Edalati, E. Akiba, Z. Horita, High-pressure torsion for new hydrogen storage materials, Sci. Technol. Adv. Mater. 19 (1) (2018) 185–193, https://doi.org/10.1080/14686996.2018.1435131.
[12] S.I. Towata, T. Noritake, A. Itoh, M. Aoki, K. Miwa, Effect of partial niobium and iron substitution on short-term cycle durability of hydrogen storage Ti-Cr-V alloys, Int. J. Hydrogen Energy 38 (7) (2013) 3024–3029, https://doi.org/10.1016/j.ijhydene.2012.12.100.
[13] E.M. Dematteis, D.M. Dreistadt, G. Capurso, J. Jepsen, F. Cuevas, M. Latroche, Fundamental hydrogen storage properties of TiFe-alloy with partial substitution of Fe by Ti and Mn, J. Alloys Compd. 874 (2021), 159925, https://doi.org/10.1016/j.jallcom.2021.159925 [Online]. Available:.
[14] J. Manna, B. Tougas, J. Huot, First hydrogenation kinetics of Zr and Mn doped TiFe alloy after air exposure and reactivation by mechanical treatment, Int. J. Hydrogen Energy 45 (20) (2020) 11625–11631, https://doi.org/10.1016/j.ijhydene.2020.02.043.
[15] A.K. Patel, A. Duguay, B. Tougas, C. Schade, P. Sharma, J. Huot, Microstructure and first hydrogenation properties of TiFe alloy with Zr and Mn as additives, Int. J. Hydrogen Energy 45 (1) (2020) 787–797, https://doi.org/10.1016/j.ijhydene.2019.10.239.
[16] V. Dixit, J. Huot, Investigation of the microstructure, crystal structure and hydrogenation kinetics of Ti-V-Cr alloy with Zr addition, J. Alloys Compd. (2019) 1115–1120, https://doi.org/10.1016/j.jallcom.2019.01.292.
[17] T. Kumar Das, A. Kumar, P. Ruz, S. Banerjee, V. Sudarsan, Hydrogen storage properties of Ti2FeV BCC solid solution, J. Chem. Sci. 131 (9) (2019) 1–8, https://doi.org/10.1007/s12039-019-1674-x.
[18] K. Nomura, E. Akiba, H2 Absorbing-desorbing characterization of the Ti-V-Fe alloy system, J. Alloys Compd. 231 (1995) 513–517.
[19] E. Akiba, Hydrogen-absorbing alloys 4 (1999) 267–272.
[20] A.D.M. Amariz, INVESTIGAÇÃO ESTRUTURAL E DA CINÉTICA DE ABSORÇÃO DE HIDROGÊNIO EM LIGAS A BASE DE TiCr, 2012.
[21] L. Pickering, D. Reed, A.I. Bevan, D. Book, Ti-V-Mn based metal hydrides for hydrogen compression applications, J. Alloys Compd. 645 (S1) (2015) S400–S403, https://doi.org/10.1016/j.jallcom.2014.12.098.
[22] S. Basak, K. Shashikala, P. Sengupta, S.K. Kulshreshtha, Hydrogen absorption properties of Ti-V-Fe alloys: effect of Cr substitution, Int. J. Hydrogen Energy 32 (18) (2007) 4973–4977, https://doi.org/10.1016/j.ijhydene.2007.06.022.
[23] S. Suwarno, J.K. Solberg, J.P. Maehlen, B. Krogh, V.A. Yartys, Influence of Cr on the hydrogen storage properties of Ti-rich Ti-V-Cr alloys, Int. J. Hydrogen Energy 37 (9) (2012) 7624–7628, https://doi.org/10.1016/j.ijhydene.2012.01.149.
[24] A. Kamble, P. Sharma, J. Huot, Effect of doping and particle size on hydrogen absorption properties of BCC solid solution 52Ti-12V-36Cr, Int. J. Hydrogen Energy 42 (16) (2017) 11523–11527, https://doi.org/10.1016/j.ijhydene.2017.02.137.
[25] T. Bibienne, V. Razafindramanana, J.L. Bobet, J. Huot, Synthesis, characterization and hydrogen sorption properties of a Body Centered Cubic 42Ti-21V-37Cr alloy doped with Zr7Ni10, J. Alloys Compd. 620 (2015) 101–108, https://doi.org/10.1016/j.jallcom.2014.08.156.
[26] M. Balcerzak, M. Wagstaffe, R. Robles, M. Pruneda, H. Noei, Effect of Cr on the hydrogen storage and electronic properties of BCC alloys: experimental and first-principles study, Int. J. Hydrogen Energy 45 (2020) 28996–29008, https://doi.org/10.1016/j.ijhydene.2020.07.186.
[27] A. Kumar, K. Shashikala, S. Banerjee, J. Nuwad, P. Das, C.G.S. Pillai, Effect of cycling on hydrogen storage properties of Ti2CrV alloy, Int. J. Hydrogen Energy 37 (4) (2012) 3677–3682, https://doi.org/10.1016/j.ijhydene.2011.04.135.
[28] A. Martínez-Amariz, D. Bellon, Effect of adding ZrM (M=Fe, Ni) intermetallic compounds on the hydrogen absorption/desorption properties of TiCr1.1V0.9 alloy, Heliyon 8 (3) (2022), 1–7, https://doi.org/10.1016/j.heliyon.2022.e09042.

[29] A. Kumar, S. Banerjee, C.G.S. Pillai, S.R. Bharadwaj, Hydrogen storage properties of Ti2-xCrVMx (M = Fe, Co, Ni) alloys, Int. J. Hydrogen Energy 38 (30) (2013) 13335–13342, https://doi.org/10.1016/j.ijhydene.2013.07.096.
[30] A. Kamble, P. Sharma, J. Huot, Effect of addition of Zr, Ni, and Zr-Ni alloy on the hydrogen absorption of Body Centred Cubic 52Ti-12V-36Cr alloy, Int. J. Hydrogen Energy 43 (15) (2018) 7424–7429, https://doi.org/10.1016/j.ijhydene.2018.02.106.
[31] H.C. Lin, K.M. Lin, K.C. Wu, H.H. Hsiung, H.K. Tsai, Cyclic hydrogen absorption-desorption characteristics of TiCrV and Ti0.8 Cr1.2 V alloys, Int. J. Hydrogen Energy 32 (18) (2007) 4966–4972, https://doi.org/10.1016/j.ijhydene.2007.07.057.
[32] J.M. Abdul, L.H. Chown, Influence of Fe on hydrogen storage properties of V-rich ternary alloys, Int. J. Hydrogen Energy 41 (4) (2016) 2781–2787, https://doi.org/10.1016/j.ijhydene.2015.11.154.
[33] J. Liu, et al., Microstructure and hydrogen storage properties of Ti–V–Cr based BCC-type high entropy alloys, Int. J. Hydrogen Energy 46 (56) (2021) 28709–28718, https://doi.org/10.1016/j.ijhydene.2021.06.137.
[34] A. Kumar, K. Shashikala, S. Banerjee, J. Nuwad, P. Das, C.G.S. Pillai, Effect of cycling on hydrogen storage properties of Ti 2CrV alloy, Int. J. Hydrogen Energy 37 (4) (2012) 3677–3682, https://doi.org/10.1016/j.ijhydene.2011.04.135.
[35] H. Hu, C. Ma, Q. Chen, Improved hydrogen storage properties of Ti2CrV alloy by Mo substitutional doping, Int. J. Hydrogen Energy 47 (2022) 1–9, https://doi.org/10.1016/j.ijhydene.2022.01.212.
[36] W. Liu, O.D. Feya, T.T. Debela, J.R. Hester, C.J. Webb, E.M.A. Gray, Experimental and computational modelling study of Ni substitution for Fe in Zr3Fe and its hydride, J. Alloys Compd. 781 (2019) 131–139, https://doi.org/10.1016/j.jallcom.2018.12.054.
[37] B.O. Mukhamedov, et al., Thermodynamic and physical properties of Zr3Fe and ZrFe2 intermetallic compounds, Intermetallics 109 (July 2018) (2019) 189–196, https://doi.org/10.1016/j.intermet.2019.01.018.
[38] S.F. Matar, a.F. Al Alam, D. Gédéon, N. Ouaini, Changes in electronic, magnetic and bonding properties from Zr2FeH5 to Zr3FeH7 addressed from ab initio, Solid State Sci. 25 (2013) 55–62, https://doi.org/10.1016/j.solidstatesciences.2013.08.002.
[39] I.Y. Zavaliy, R.V. Denys, R. Černỳ, I.V. KovaL'Chuck, G. Wiesinger, G. Hilscher, Hydrogen-induced changes in crystal structure and magnetic properties of the Zr3MOx (M = Fe, Co) phases, J. Alloys Compd. 386 (1–2) (2005) 26–34, https://doi.org/10.1016/j.jallcom.2004.05.064.
[40] F. Stein, G. Sauthoff, M. Palm, Experimental determination of intermetallic phases, phase equilibria, and invariant reaction temperatures in the Fe-Zr system, J. Phase Equil. 23 (6) (2002) 480–494, https://doi.org/10.1361/105497102770331172.
[41] A.A. Coelho, TOPAS and TOPAS-Academic: an optimization program integrating computer algebra and crystallographic objects written in C++, J. Appl. Crystallogr. 51 (1) (2018) 210–218, https://doi.org/10.1107/S1600576718000183.